Observation of internal tides, nonlinear internal waves and mixing in the Lombok Strait, Indonesia

Adi Purwandana, Yannis Cuypers, Pascale Bouruet-Aubertot

Version of Record: https://www.sciencedirect.com/science/article/pii/S0278434321000157
Manuscript_e6072fdd8da300c614e5e32b9d4c3e11

Observation of internal tides, nonlinear internal waves and mixing in the Lombok Strait, Indonesia

Adi Purwandana[1,2)], Yannis Cuypers[1)], Pascale Bouruet-Aubertot[1)]

[1)]Laboratoire d'Océanographie et de Climatologie par Expérimentation et Approche Numérique (LOCEAN), Sorbonne Université, Paris, France

[2)]Research Center for Oceanography, Indonesian Institute of Sciences (RCO-LIPI), Jakarta, Indonesia

Corresponding author: adip001@lipi.go.id

Abstract

Lombok Strait is one of the main exit passages of the Indonesian throughflow (ITF), connecting the interior Indonesian seas with the Indian Ocean. Satellite images have shown that this strait is also the most remarkable zone of the Indonesian seas for the generation of internal tides, which frequently evolve into internal solitary waves (ISWs). Here we present the first comprehensive high-frequency observations of the internal tide in the strait. The observations were carried out at a fixed position around 8 km from the western coast of Lombok Island at a depth of ~300 m. We confirmed the appearance of the non-linear internal tide with an amplitude of ~90 m at a fairly close distance (~30 km) from its generation site in the Nusa Penida Sills (NPS), with a dominant M_2 tidal frequency. High-frequency internal waves associated with vertical velocities reaching 20 cm s^{-1} were observed within the internal tidal trough. We estimated the turbulent kinetic energy dissipation rate using Thorpe and Ellison scales and found a mean dissipation rate of the order of ~ [10^{-6}-10^{-7}] m^2 s^{-3}, with enhanced values in the thermocline layer, possibly driven by shear instabilities. We underlined that the use of the Ellison scale is a promising alternative for indirectly estimating the dissipation rate from high-resolution time-series data sets.

Keywords: Indonesian seas, internal solitary wave, Lombok Strait, dissipation rate, mixing

1. Introduction

The Indonesian seas connect the Pacific and Indian Oceans and represent a key passage of the Thermohaline Circulations (Gordon, 2005; Gordon and Fine, 1996). One of the most important

exit passages of the Indonesian throughflow (ITF) is the Lombok Strait, located in the Lesser Sunda Islands waters. This strait separates the Bali and Lombok Islands, between 115.3°-116.1° E and 8.2°-8.7° S and connects the Kangean waters (western Flores Sea) in the north, and the Indian Ocean in the south. The Lombok Strait is part of the western route of the ITF, a bypass that connects directly the ITF flowing from the Makassar Strait after passing the Dewakang waters. The flow through this strait represents 20% of the ITF (Hautala et al., 1996). In situ measurements in this strait from January 1985 to January 1996 (Murray and Arief, 1988) show an average transport of 1.7 Sv (1 Sv = 1×10^{-6} m^3s^{-1}) with a maximum of 3.8-4.0 Sv towards the Indian Ocean during July and August 1985; and the minimum within 0-1 Sv is observed from December 1985 to January 1986. The flow in the Lombok Strait is controlled by the presence of the Nusa Penida Sill (hereinafter NPS) which reaches 350 m depth (Murray and Arief, 1988). The circulation of water masses underneath the Pacific water mass is restricted by the NPS.

The Lombok Strait basin is dominated by Pacific water masses, i.e. the North Pacific subtropical water (NPSW), fed by the Makassar Strait throughflow and characterized by σ_θ = 24.5 kg m^{-3} at 100-200 m depth (Hautala et al., 1996; Wyrtki, 1961). This strait waters have distinctive characteristics compared to other exit passages along the Lesser Sunda Islands chain. The salinity in the Lombok Strait is influenced by the fresher water from the Java Sea and by local precipitation during Northwest Monsoon (December-May). A freshening, which can exceed 2 PSU, occurs from March to May (Sprintall et al., 2003).

Spatial variation in the hydrodynamics of the Lombok Strait is unique. The flow in the Lombok Strait shows a strong layered structure with a permanent southward flow in the upper layer and a reversing southward-northward flow in the lower layer (Hautala et al., 2001). The upper southward flow is maximum in March-April while the reversing northward flow is maximum in May. The southward flow is controlled by the low-frequency component of the large-scale wind forcing from the Pacific Ocean; while the lower layer reversing flow is correlated with semi-annual Kelvin wave events forced by westerly winds during the Northwest to Southeast Monsoon

53 transition period (November/December and April/May) in the equatorial Indian Ocean (Potemra et
54 al., 2002; Sprintall et al., 2003). Since the strait opens directly onto the Indian Ocean, the northward
55 lower layer flow generated by Kelvin waves can result in intrusions of the Indian Ocean waters
56 (Sprintall et al., 1999; Susanto et al., 2001; Wijffels et al., 2002). The throughflow in the Lombok
57 Strait also varies longitudinally. The stronger southward flow is observed in the western side of the
58 strait, a phenomenon related to the higher sea level height on the Lombok Island side than that on
59 the Bali Island side (Hautala et al., 2001; Murray and Arief, 1988).

60 The strong mixing of Pacific watermass observed in the Indonesian seas generates cold
61 surface anomalies and fresh pycnocline anomalies, which impacts the Indian and Pacific heat and
62 freshwater budgets (Lee et al., 2002) as well as local deep atmospheric convection and wind
63 regimes (Koch-Larrouy et al., 2010). This mixing is mainly driven by internal tide induced
64 turbulence as shown by previous in situ observations (Bouruet-Aubertot et al., 2018; Koch-Larrouy
65 et al., 2015; Purwandana et al., 2020; Robertson and Ffield, 2005), satellite images of sea surface
66 temperature (Ray and Susanto, 2016) and modeling studies (Hatayama, 2004; Koch-Larrouy et al.,
67 2007; Nagai et al., 2017; Nagai and Hibiya, 2015; Nugroho et al., 2018; Schiller, 2004). Internal
68 tides are generated in stratified waters when the tidal flow encounters a topographic feature. A
69 vertical motion is induced, and the oscillating water mass will be subjected to the buoyancy and
70 Coriolis restoring force. In the Indonesian seas, tidal mixing is particularly intense over rough
71 topography, such as in the Lifamatola, Manipa, Ombai, and Lombok Straits, and the Sibutu Island
72 chains (Purwandana et al., 2020).

73 The tide in the Lombok Strait is produced by tidal waves propagating from the Indian Ocean
74 with a dominant M_2 semi-diurnal period of 12.4 hours. The tidal flow can reach ± 3.5 m s^{-1} in the
75 sill area (Murray and Arief, 1988). Numerical simulations have shown a strong conversion of
76 semidiurnal M_2 barotropic to baroclinic internal tides around the NPS (Nagai and Hibiya, 2015;
77 Nugroho et al., 2018) which shows that the Lombok Strait is a strong mixing hot spot. The 1/100°
78 simulation map of the M_2 internal tides energy flux and depth-integrated dissipation is reproduced

79 in **Figure 1**a evidencing the strong northward M_2 internal tides fluxes as well as the region of very
80 strong dissipation at the sill and along the eastern coast of Bali and western coast of Lombok.
81 Analysis of satellite sea surface temperature also revealed a spring neap cycle in the Lombok Strait
82 evidencing strong mixing associated with tides there (Ffield and Gordon, 1996; Ray and Susanto,
83 2016).

84 Strong amplitude internal tides generally evolve non linearly into steep front and trains of
85 short-scale large amplitude solitary waves. Such solitary waves trains can transport energy far away
86 from the generation site and to dissipate it when they shoal at continental slopes. This process has
87 important consequences for local biogeochemical dynamics (Bourgault et al., 2014). Two typical
88 situations are encountered, when the flow at the sill is always subcritical, ($Fr = U_{bar}/c<1$) with U_{bar}
89 the barotropic tidal velocity and c the internal mode phase speed, the internal tides steepens
90 progressively as it propagates away from the sill and then breaks down into solitary waves train
91 under the effect of non-hydrostatic dispersion (Gerkema and Zimmerman, 1995). This is the first
92 process that is believed to take place in the extensively studied, Luzon Strait region (South China
93 Sea) (Alford et al., 2015). When the flow gets supercritical at the sill, the wave propagation is
94 impeded a depression grows and is released when the tide slackens, the depression then rapidly
95 breaks into a train of solitary waves. This second mechanism, known as the lee waves mechanism,
96 has been observed in several well know Internal Solitary Waves (hereinafter ISWs) generations sites
97 such as the Strait of Messina (Brandt et al., 1999) or the Sulu Sa (Apel et al., 1985). The strong
98 Lombok Strait internal tides can evolve into a train of large vertical displacement (~100m) small
99 horizontal scale (~km) ISWs (Aiki et al., 2011; Matthews et al., 2011). The model of Nagai and
100 Hibiya (2015) also indicates that the northward propagating energy flux is stronger than that of the
101 southward favoring ISW propagating northward (**Figure 1**a). ISW indicators are often observed
102 from satellite images as sea surface alternating bands of slicks and rough patches propagating from
103 NPS and became a classical illustration of ISW observation from space (see Jackson, 2007). Yet, the
104 only in situ observation of internal solitary waves in the Lombok Strait is a short snapshot of an

echosounder by Susanto et al. (2005) evidencing an impressive solitary wave of ~150 m vertical displacement. Satellite and numerical-based studies in the Lombok Strait revealed that the Lombok ISWs propagate predominantly northward of the strait (Aiki et al., 2011; Matthews et al., 2011). Their studies also suggest that the ITF tends to reduce the frequency and occurrence of ISW. The strong barotropic tidal velocities at the sill also suggest that the ISW are rather generated through the lee waves mechanism.

Here, we present the first high-frequency observations of the non-linear internal tides and associated high-frequency waves in the Indonesian seas, i.e. in the Lombok Strait. We characterize the impact of internal tides and high-frequency waves on turbulence in the pycnocline using both the Thorpe scale method applied to CTD profiles and the Ellison scale method applied to high-frequency time series of temperature sensors.

This paper is organized as follows. Section 2 describes the observation dataset and methods to derive the mixing estimates from observations. We put the detail of the method in the Appendix. Section 3 presents results and discussion gained from observations, including the analysis of the characteristics of the observed ISW and mixing estimates induced by internal tides. The results are summarized in section 4.

2. Methodology

2.1 In situ Observations

A field experiment was conducted during a spring tide period at the transition between Southeast Monsoon and Northwest Monsoon, on 3-5 November 2017 in the Lombok Strait waters at a fixed position, 8.56^{o} S, 116.02^{o} E offshore of the west coast of Lombok Island (~8 km) at a depth of 300 m during the transition from neap to spring tide (red star in **Figure 1**a). The field experiment was conducted from a small anchored boat, which precluded a deep location in the middle of the channel or too close to the sill because of the very strong currents. This location is thus appropriate for characterizing possible enhanced dissipation resulting from ISW interaction

with the shore but does not allow to characterize the most coherent unaltered ISW structure near their generation site. A detailed description of the measurements is shown in **Table 1**.

Table 1 Available in situ measurements in the Lombok Strait, 3-5 November 2017.

Date	Hour of CTD casts (GMT+8)	Other operated instruments
November 3rd, 2017	15.23; 18.18; 19.28; 21.24; 23.38	ADCP, RCM, EK80, RBRs
November 4th, 2017	02.12; 03.39; 04.30; 07.20; 09.27; 11.10; 13.25; 15.28; 15.46; 16.08; 18.40; 21.19	
November 5th, 2017	00.14; 02.07; 04.06; 04.26; 04.45; 07.18; 07.46; 08.00; 10.30; 12.22	

High-frequency imaging of the internal wave structure was obtained using a 200 kHz narrow-beam echosounder Simrad EK80 that covered up to 150 m depth. A 0.75 MHz downward-looking *Sontek* Acoustic Doppler Current Profiler (ADCP) was moored on a floater connected to the anchored boat. The instrument was lowered at a depth around 50 m and measured the currents down to ~100 m depth with 5 m bin resolution and 1 minute time averaging. An *Anderaa Seaguard* RCM was also deployed at the depth of ~150 m to get the current variability in the deeper layer, sampling with 1-minute temporal resolution. Temperature field variability was measured at high frequency (1 Hz) using 4 RBR duet sensors (temperature and pressure) and 2 RBR solo sensors (temperature only) that were attached at several depths between 80 m and 270 m. Note that the internal tide motion-induced large heaving of the mooring instruments, hence the portion of the water column sampled was not constant. Moreover, the mooring was anchored to the boat but could oscillate horizontally with an amplitude of ~100 m. The instantaneous absolute velocities can be biased by this motion, and for this reason, we consider only in the analysis the horizontal shear and the time mean velocity where high-frequency oscillations of the ADCP position around the boat are smoothed out. Temperature and salinity profiles were collected using a *Sea-Bird Electronics* (SBE) CTD 19 Plus from the surface to depths of ~200 m around every two hours and 2-3 yoyo casts were repeated when a sequence of internal waves was observed in the echosounder. The profiles were de-

spiked and averaged into 0.5 m using the SBE data processing modules. Data above 5 m were removed due to contamination of the CTD probe soaking effect and ship's wake. Predicted tidal height, zonal and meridional current components gained from Oregon State University tidal inversion software (OTIS) (Egbert and Erofeeva, 2002), including the observation time in the Lombok Strait and field observation design is shown in **Figure 1**c-e.

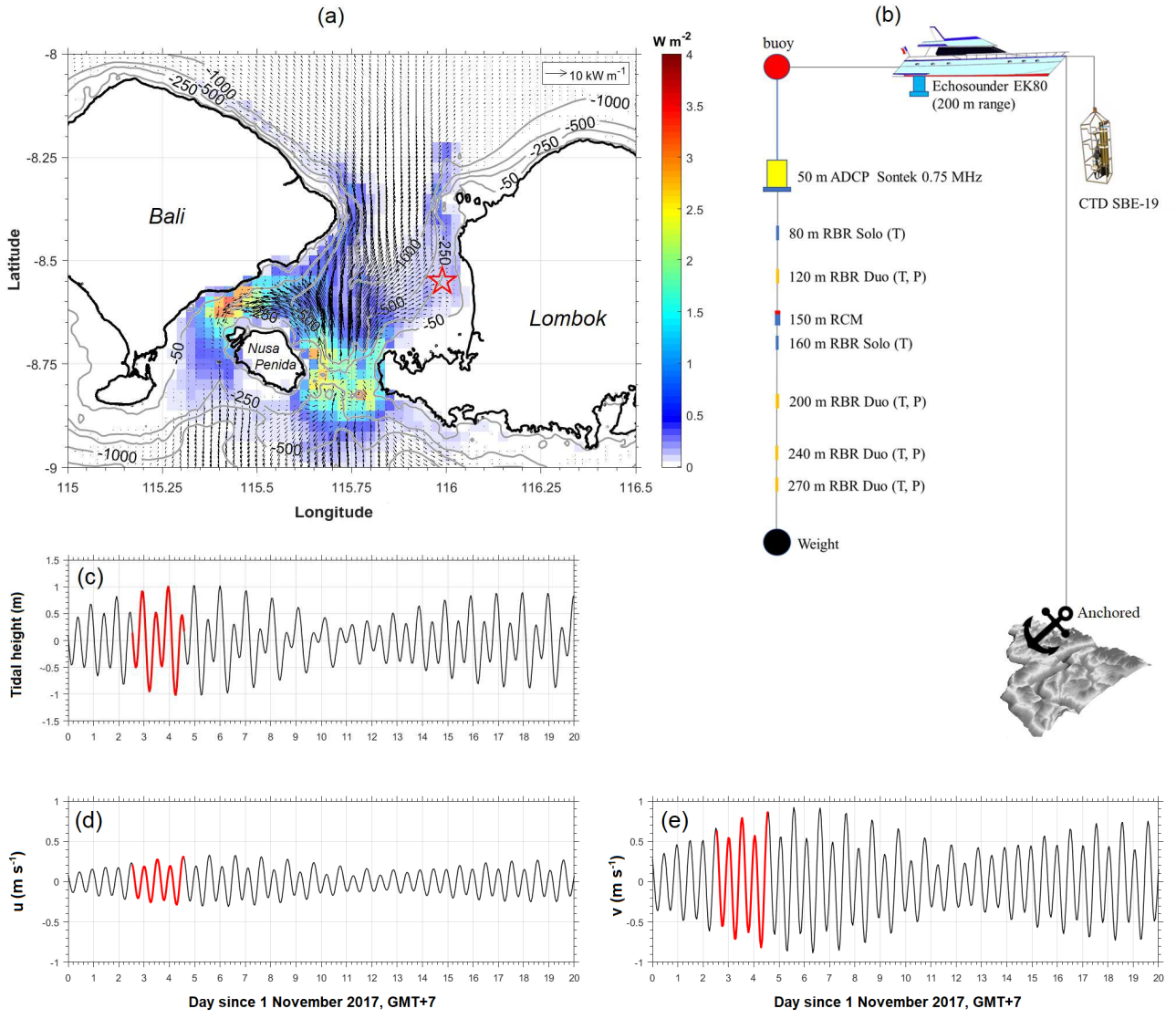

Figure 1 (a) A 0.025° grid averaged of the depth-integrated semidiurnal M_2 driven turbulent kinetic energy (TKE) dissipation rate (colored plot, W m^{-2}) and depth-integrated M_2 baroclinic energy flux (arrows, kW m^{-1}) inferred from a 3D hydrostatic model by Nagai and Hibiya (2015) (personal communication) in the Lombok Strait. The bathymetry is provided by the Gebco_08 grid. The red star is the observation site. (b) The measurements scheme, which involved ADCP, CTD,

echosounder and RBR sensors, (c, d, e) is the predicted tidal height, zonal current (u), and meridional current (v), respectively on 1-20 November 2017 above the Nusa Penida sills. Red lines indicate the timing of field observation on 3-5 November 2017.

2.2 Mixing estimates

Turbulence dissipation rates were inferred using both an improved Thorpe scale (L_{Th}) method (Purwandana et al., 2020) and Ellison scale (L_E) method from the CTD casts and high temporal resolution temperature sensors at a fixed depth measured by moored instruments, respectively. Both Thorpe and Ellison methods are indirect estimates to infer the dissipation rates based on the detection of the largest turbulent eddies signature. Both methods rely on the assumption of a statistical linear relationship between the largest overturns size and the Ozmidov scale (Mater et al., 2015). The Ozmidov scale is a theoretical dynamical scale directly related to the turbulent energetics through ε as $L_o=\varepsilon^{(1/2)}N^{(-3/2)}$. A turbulent overturn will have a signature in term of density inversion along z for a given time (Thorpe method) and high-frequency density oscillation at a given depth (Ellison scale method). For both methods, we have used temperature as a proxy for density, as justified in the Appendix. For the Thorpe method we obtain an estimation of the largest overturns size from the standard deviation of density inversions (built from temperature), while for the Ellison scale method, the largest overturn size is obtained from the standard deviation of turbulent time fluctuations of temperature divided by the mean temperature gradient.

The Ellison method estimation of the dissipation rate was found comparable to the microstructure measurements direct estimates according to a study by (Moum, 1996); yet as stated by Cimatoribus et al. (2014), the Ellison scale may overestimate/underestimate the real turbulence dissipation rate during the initial stage/late stage of the turbulence decay. The Thorpe method uses a single temperature/density profile and inspects turbulent events represented by overturning events where the denser parcel lies above the less dense parcel. The Ellison method inspects turbulence events from high-resolution time-series measurements and inspects any fluctuations which are expected to be related to turbulence once this signal is decomposed into some possible sources:

surface waves, internal waves and turbulent events. . In our case, the screening for the temperature is crucial to omit any spurious fluctuations related to the high-frequency surface waves and internal waves (see Appendix). Our dissipation rate estimate by employing the time series data sets using the Ellison scale method is similar to a study by Cimatoribus et al. (2014). The detailed processing for Thorpe and Ellison scale method is provided in the Appendix.

3. Results and Discussion

3.1 Hydrography

Our observations were conducted during a transition period from the Southeast Monsoon to the Northwest Monsoon. The stratification derived from the CTD profiles shows a thick pycnocline extending between 50 and 150 m with a maximum stratification near 85 m depth (**Figure 2**d). The time-mean currents (over the four M_2 tidal periods recorded) show a strongly sheared structure with strong background westward-eastward zonal current of ~0.3 m s^{-1} and northward-southward meridional current of ~0.5 m s^{-1} (**Figure 2**c). We suggest that the southward currents are related to the ITF current, while the northward currents are presumably influenced by semi-annual Kelvin wave events, which appear during the Southeast Monsoon transition period (November/December and April/May) (Sprintall et al., 2003, 1999; Susanto et al., 2001; Wijffels et al., 2002). The time-mean squared shear measured by the ADCP between 55 and 100 m shows strong values exceeding the N^2 values and leading to near-critical *Ri* values.

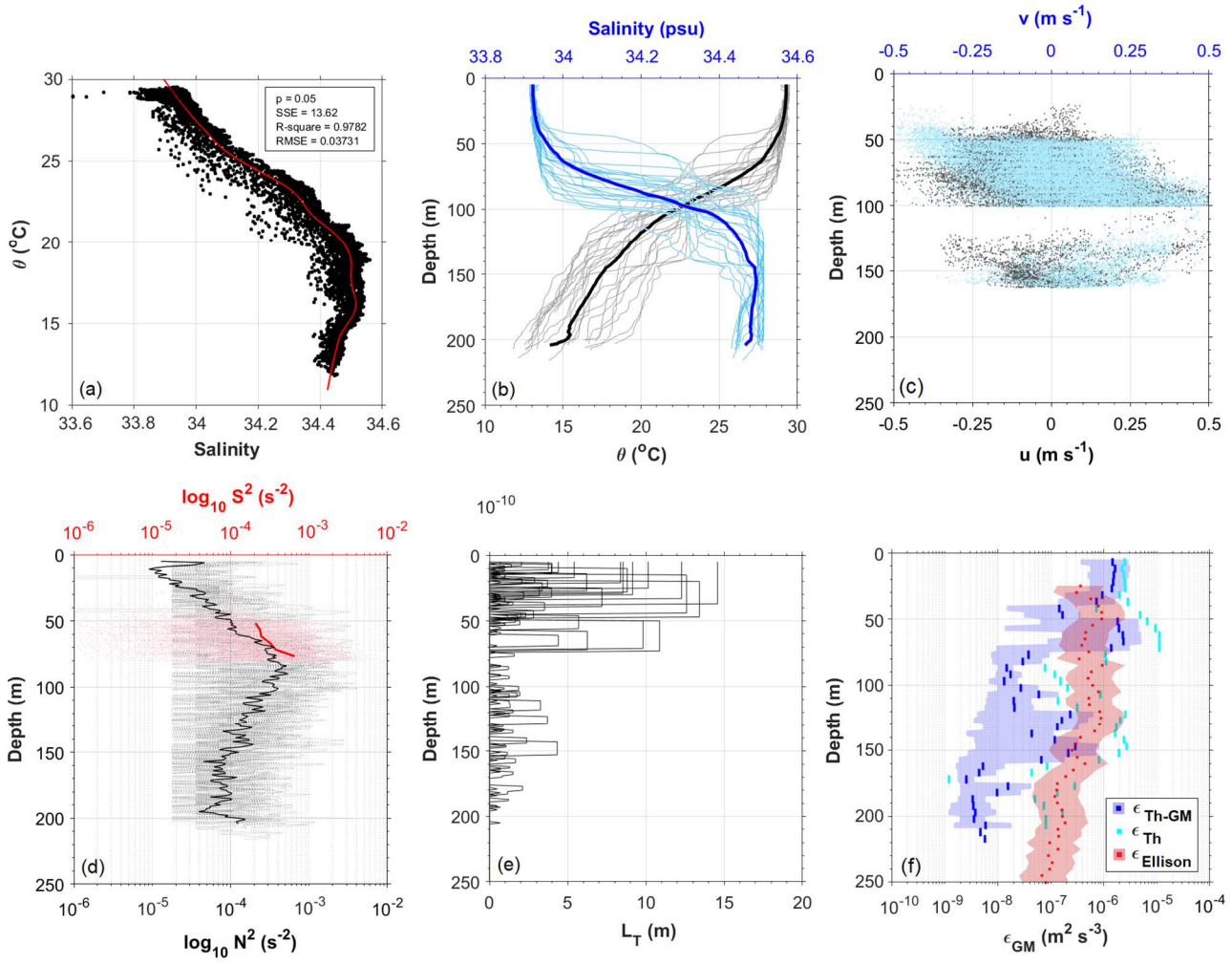

205

206 **Figure 2** (a) Temperature-salinity relationship inferred using spline fit with the goodness values are
207 indicated, (b) potential temperature and salinity profiles (grey and light blue lines, respectively)
208 with its mean values (black and blue lines, respectively); (c) zonal, *u* and meridional, *v* (grey and
209 light blue plots, respectively); (d) the squared buoyancy and squared shear profiles (black and red
210 plots, respectively) with its mean values (lines), (e) the Thorpe length; (f) the 10 m mean dissipation
211 rate with background Garrett-Munk (GM) dissipation rate applied (blue), without background GM
212 dissipation (cyan) and that of the 10 m running mean dissipation values inferred using Ellison scale
213 (red). The shading plot for the GM-Thorpe and Ellison estimates in (f) indicates the 95% confidence
214 intervals values for each bin.

215 The time series of temperature recorded from the mooring sensors show a clear non-linear
216 semi-diurnal signal characterized by semi-diurnal periodic large troughs (**Figure 3**a). The peak to
217 peak amplitude reaches ~90 m for the 20°C isotherm located in the pycnocline, which is larger than

internal tides observed in the Makassar Strait and Buru Strait (Purwandana et al., 2020); Seram Sea, and Flores Sea (Ffield and Robertson, 2008); and comparable to the largest observed internal tides in the North Halmahera Sea and Ombai Strait, which were associated to very large turbulent dissipation rates (Bouruet-Aubertot et al., 2018). The low pass filter (period >3 hours) of 18°, 20°, 22° C isotherms time series show that each M_2 period is composed of one large trough (T_0) of ~70 m and two smaller troughs (T_1, T_2) of ~20 m, evidencing higher harmonics (M_4, M_6) in the signal.

3.2 ISWs characteristics

The barotropic velocities predicted by the OTIS model (Egbert and Erofeeva, 2002) over the NPS, U_{bar}, reach ~0.9 m s^{-1} during the period we sampled, while the mode-1 phase speed, c_1 is typically of 1 m s^{-1}. This gives the Froude number, $Fr = U_{bar}/c_1$, close to supercritical hence it is expected that ISW are generated by the lee waves mechanism (Maxworthy, 1979). Numerical experiments study (Aiki et al., 2011) and satellite observation images (Astawa Karang et al., 2012) show that an ISW packet can already be formed at about 10-20 km from NPS which is consistent with a rapid formation by a lee wave mechanism. In our observations, high-frequency waves are observed almost continuously, but the largest amplitude wave-packet is observed in the large trough of the second tidal period (**Figure 3** event B). A significant wave packet is also observed during the third period (**Figure 3** event C) but no clear wave packet is observed within the large trough of the first and fourth periods. The waves generated during these events have a strong vertical coherency, a maximum amplitude of ~40 m, a short period of 9-12 minutes, and are associated with strong vertical velocities reaching 20 cm s^{-1}. The wave packet A has also a clear signature in the echo-sounder, consistent with the isotherms displacements. The echo-sounder signal for packet B was unfortunately too noisy to be exploited. The high frequency waves induce a clear heaving of a background strongly layered shear. Since the high frequency waves are highly coherent vertically, they do not likely contribute to this small-scale (~20 m vertical scale) shear structure. This background shear structure may result from the interaction of internal tide, ITF, Kelvin waves and possibly near inertial waves, but our measurements period is too short to characterize them.

244 Distinct high-frequency wave packets are also generated on the front face of T_2 (as shown
245 by the close up A and D) and are likely generated by the higher tidal harmonics composing the
246 internal tide. They are characterized by a longer wave period of ~20 minutes and smaller maximum
247 amplitude of ~20 m. They are associated with weaker vertical velocities of ~5 cm s^{-1}. They also
248 induce clear heaving of the small-scale shear structure.

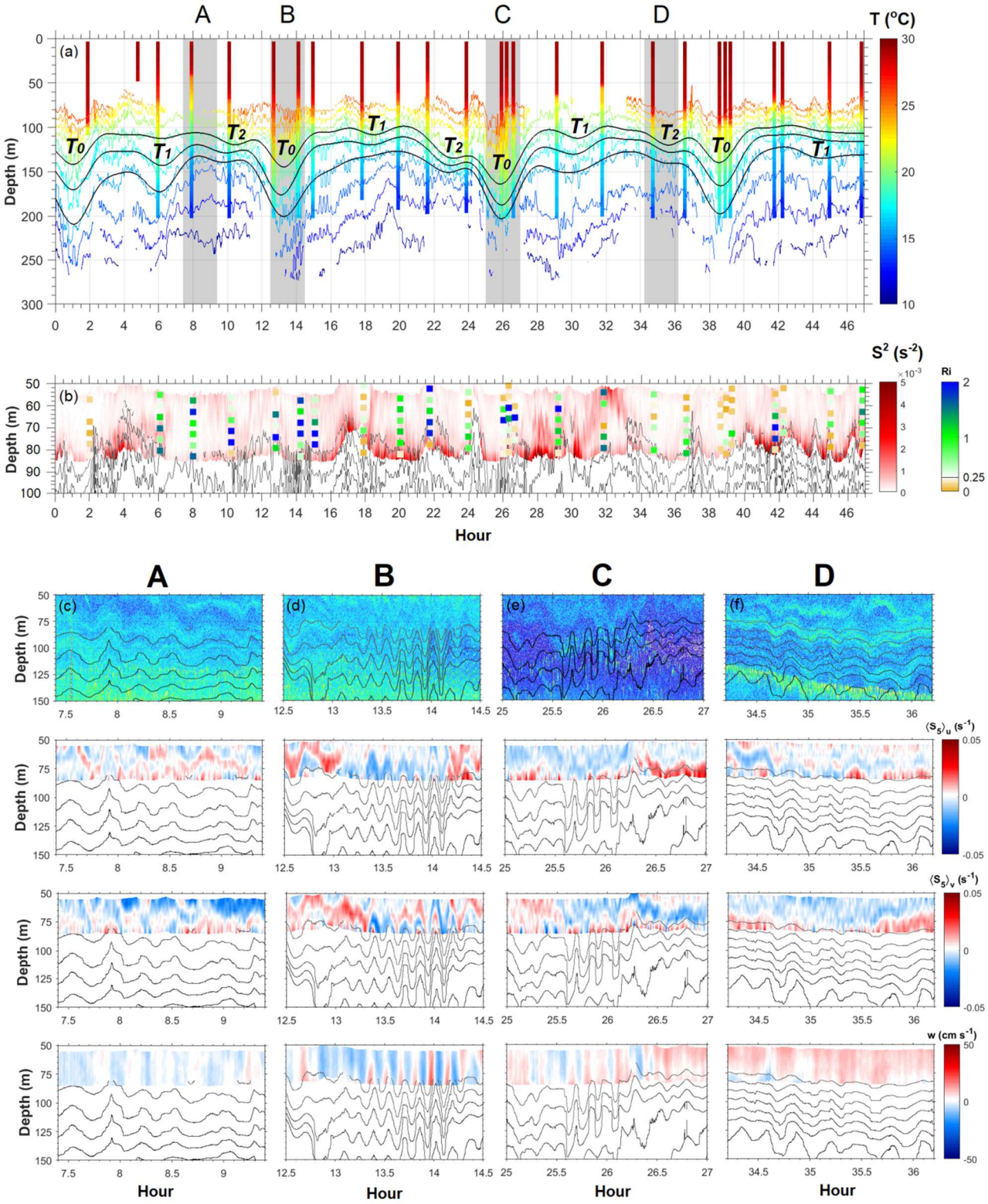

Figure 3 (a) Isotherm contours inferred from RBR sensors and temperature profiles from CTD casts. The black line is low pass filtered (>3h) for isotherms 18, 20, and 22° C. (b) The squared shear with isotherms and Richardson number, *Ri* superimposed. (c, d, e, f) The enlarged view of shaded areas A, B, C, and D in (a) for echosounder image (in arbitrary unit) in the first upper panel, zonal shear, $(S_5)_u$, meridional shear $(S_5)_v$ and vertical current *w*. Enlarged images for annotated areas

A, B, C, and D denote the appearance of shortperiod internal waves (B, C) and longer period internal waves (A, D). T_0 and (T_1, T_2) are the large and the small troughs, an indication of M_2 and higher harmonic signals (M_4, M_6), respectively.

The phasing of the largest high-frequency waves (events B, C) with the large troughs is consistent with a lee wave mechanism, yet none of the high-frequency waves observed is rank-ordered and they do not show a typical $sech^2$ solitary waves profiles, as is generally expected from the lee wave mechanism (Apel et al., 1985; Maxworthy, 1979). This may have been the result of an interaction with the sloping topography at our observation site. **Figure 1**a shows that the modeled internal tide fluxes are indeed across the slope at our location and that the dissipation is increasing onshore suggesting strong interaction of the internal tides with the slope. In addition, the depth variation and friction effects can alter the nonlinear terms driving the solitary wave packet evolution, as was shown from classical extended KdV framework in the Northwest shelf of Australia by Holloway et al. (2002). Simulations and observations of non-rank-ordered wave packets were also reported at the Stellwagen Bank in the Massachusetts Bay in conditions of moderate to strong forcing while rank-ordered packets were recovered for weaker (neap tide) forcing (Scotti et al, 2007). Numerical and observational studies in the Gibraltar Strait by Vlasenko et al. (2009) have also evidenced frequent non-rank-ordered packets that were attributed to multiple reflections from lateral boundaries along with friction and wave breaking. They also observed that if the non-rank-ordered wave packet pursues its propagation over a flat bottom, the high-frequency waves re-order.

It is interesting to notice that satellite observations from the Himawari-8 satellite made on November, 4th between 15.30 and 16.00 LT (local time) show the propagation of a train of ISW with a clear pattern at the northern exit of the strait (**Figure 4**). These images were captured about 12 hours after we observed the main high-frequency wave packets B. The leading ISW is about 80 km from our in-situ observation location, which suggests a phase speed of ~1.9 m s^{-1}, consistent with previous estimates (Susanto et al., 2005). The decreasing satellite signal intensity from the leading

281 wave to the trailing waves suggests that the wave packet is rank-ordered when it exits Lombok
282 Strait and that the non-rank order signal we observe is a local process.

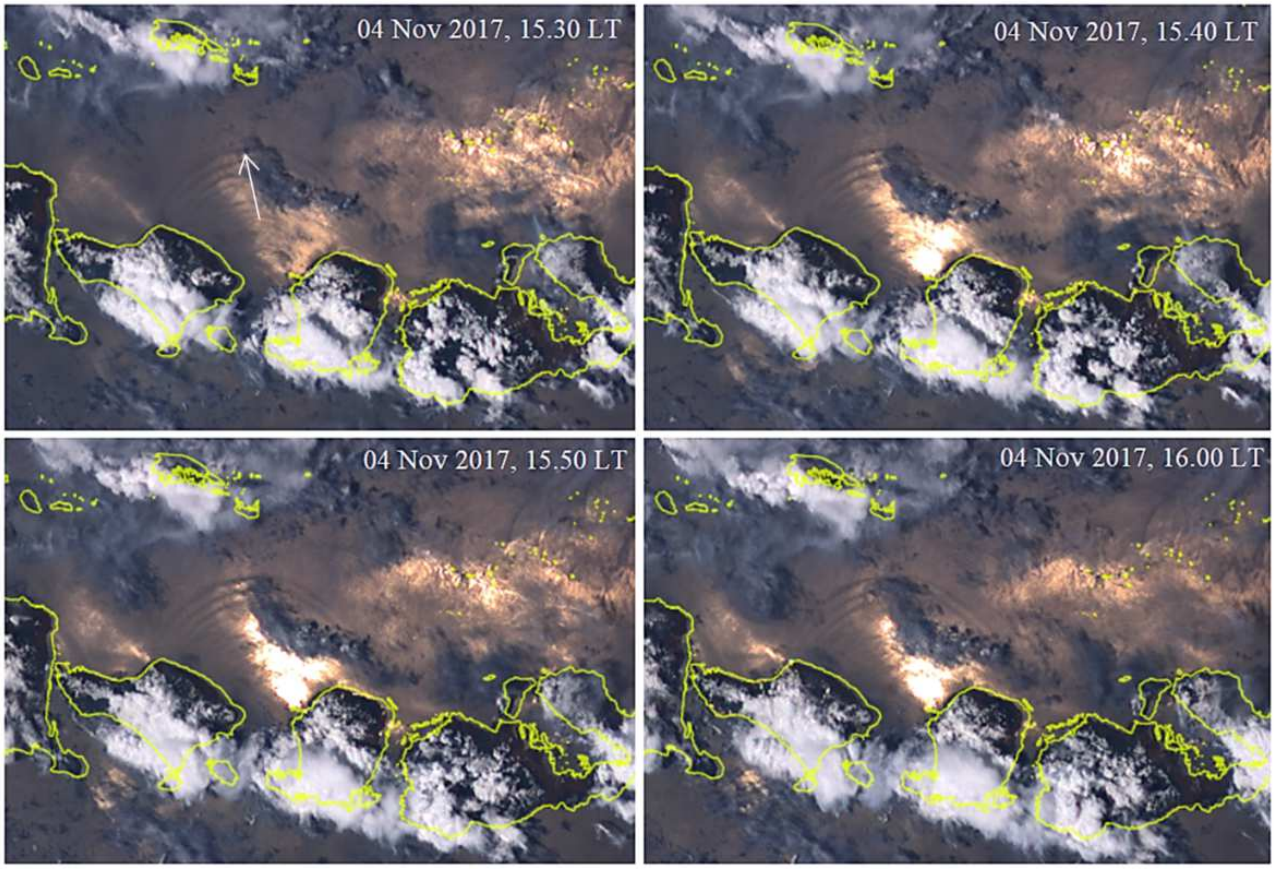

283

284 **Figure 4** The observed ISWs signature (white arrow) by satellite images Himawari-8 on November
285 4th, 2017 at: (a) 15:30 LT (GMT+8), (b) 15:40 LT, (c) 15:50 LT and (d) 16:00 LT.

286 The fact that the ISW train is weaker on the third large trough and absent on the fourth large
287 trough is surprising considering that the barotropic forcing is increasing. A similar strong variation
288 of the number of high-frequency waves from one tidal cycle to another was also reported at the
289 Stellwagen Bank (Scotti et al., 2007). According to Scotti et al. (2007), changes in stratification and
290 forcing alone could not explain this variability. The dissipation and 3D effects should be considered
291 to explain this chaotic behavior. As previously stated, these effects are likely important considering
292 that a large part of the internal tides flux is directed onshore at our location and that the dissipation
293 rate increases toward the shore.

3.3 Dissipation estimates

Our ADCP measurements within the thermocline layer as shown in **Figure 2**d show a wide range of variation of the shear. The mean value of the squared shear profile is higher than the mean of the squared buoyancy profile while the instantaneous profile shows frequent supercritical conditions ($Ri=N^2/S^2$ <0.25), which is remarkable considering that we are located in the strongly stratified thermocline. Elevated dissipation rates are observed in the temporal evolution of $\varepsilon_{\text{E-patch}}$ (**Figure 5**b), where the most persistent elevated dissipation rate occurred in the upper layer >120 m depth.

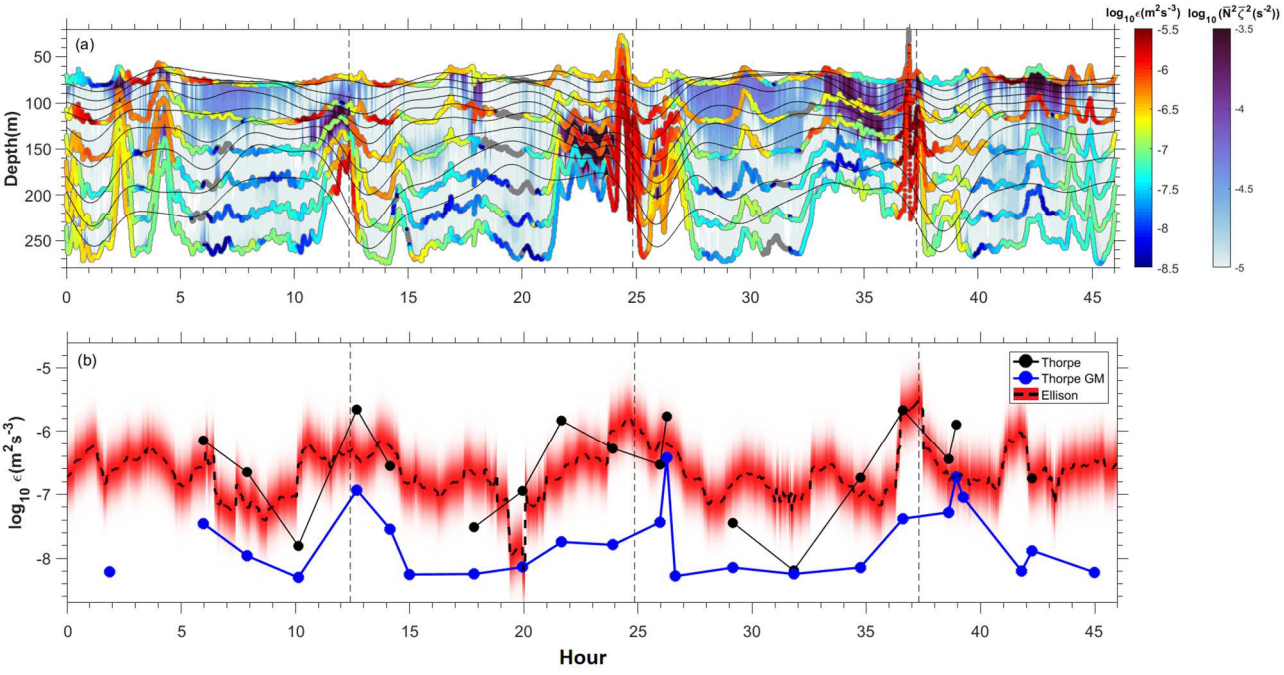

Figure 5 (a) Spatiotemporal evolution of the dissipation rate estimated using Ellison scale (ε_E) at several mooring depths (scaled in $\log_{10}$, in colored contours; note that the depth of the dissipation estimate follows the sensors displacements), the strain (scaled in $\log_{10}$, in blue-scaled contours), and the low pass filtered (>3h) isotherms (black contours); (b) mean over the depth covered by the mooring of the dissipation rates inferred using Thorpe scale patch and that considering the GM-background dissipation rate (black dotted line and blue dotted line, respectively), and using Ellison scale (dashed line for the mean and shaded red area for the confidence interval assuming the

Gaussian distribution shown in Figure A3b for the error made on the estimate of the local temperature gradient. Note that the shading intensity decreases with the probability.

The time and depth mean values of the dissipation rate result in an upper bound patch estimate of $\varepsilon_{Th\text{-}patch}=2.19\times10^{-6}$ m^2s^{-3} and its standard deviation 4.56×10^{-6} m^2s^{-3}; the lower bound GM background estimate of $\varepsilon_{Th\text{-}GM}=2.88\times10^{-7}$ m^2s^{-3} and its standard deviation 7.61×10^{-7} m^2s^{-3}; $\varepsilon_E=3.28\times10^{-7}$ m^2s^{-3} and its standard deviation 3.85×10^{-7} m^2s^{-3}. The time-mean depth profile of the dissipation rate varies in the range $[10^{-8}\text{-}10^{-6}]$ m^2s^{-3} with smaller values for the Thorpe method at the pycnocline oscillating in the range 75-120 m (see **Figure 2**f), which may result from a bias in the detection of overturns for the strongest stratification. These values characterize strong dissipation rates in the pycnocline, which can be compared to the highest thermocline dissipation rate found in the Halmahera Sea during the INDOMIX Program (Bouruet-Aubertot et al., 2018). The discrepancy between the Thorpe and Ellison methods is larger when we consider the lower bound inferred from the GM background dissipation rate estimate that results from the much less frequent detection of overturns in the CTD profiles than that of in the temperature-thermistor time series profile. The time evolution of the depth-mean dissipation rate of ε_{Th} and ε_E is shown in **Figure 5**b. A clear semi-diurnal pattern emerges with dissipation peaks exceeding 1×10^{-6} m^2s^{-3} and reaching 1×10^{-5} m^2s^{-3} observed within the large internal tide troughs (marked by vertical dashed lines in **Figure 5**b). Similar observations have been made in a different context by Xie et al. (2013) in the central Bay of Biscay where maximum dissipation is encountered in narrow troughs of the nonlinear internal tides. It is indeed expected that the front of the internal tide will be associated with a sharp increase of the velocity, velocity shear, and strain which can favor shear and/or convective instabilities. In our observations, the tidal front is associated with an initial squeezing of the isopycnals at the tidal edge followed by stretching during the tidal abrupt trough. A strong strain is notably generated during the squeezing of the isopycnal at the leading edge of the wave just preceding the abrupt fall (we have added a computation of the large-scale strain in the background of **Figure 5**a). This strain is associated with strong dissipation rates. In this study, the background scaled-strain is derived from

the temperature sensors as $\bar{N}^2\,\bar{\zeta}^2$ with $\zeta = (N^2 - \bar{N}^2)/\bar{N}^2$, N^2 is the time varying stratification computed from the temperature derived potential density and $\bar{N}^2$ is its time average. Similar periodic strain/dissipation increase has been described by Klymak et al. (2008) in the vicinity of the deep Kaena ridge where strong internal tides are generated. They attributed this periodic dissipation to direct breaking resulting from convective instabilities. Unfortunately, our ADCP sampling is of limited range so that we can not determine the *Ri* number below ~90 m depth to characterize the possible onset of shear instabilities or local *Fr* number for convective instabilities. In any case, the phase lock of the dissipation with the tides suggests a rapid "direct" breaking mechanism as opposed to a weak wave-wave interaction mechanism as parameterized by the Gregg-Henyey-Polzin (hereinafter GHP) parameterization (Polzin et al., 2014). This is in agreement with the conclusions of Bouruet-Aubertot et al. (2018) and Klymak et al. (2008) that the GHP parameterization may not be valid in the near field of the internal tides. The time series of the dissipation rate from the Ellison estimate also shows a decreasing trend of the dissipation rate with depth, with the higher values observed for the two shallower temperature sensors (80 and 120 m average depth) surrounding the pycnocline peak where frequent supercritical conditions are observed from shear measurements.

4. Summary

We provide the first high-frequency in-situ observations of strong semi-diurnal internal tides (~90 m amplitude) in the Lombok Strait at a short distance of about 30 km from the generation source at the Nusa Penida Sill. Frequent signatures of high frequency (10-20 minutes period), high vertical velocity internal wave trains are observed. The largest high-frequency wave packets (with waves reaching up to 40 m) are observed within the M_2 periodic large internal tide trough, but weaker high-frequency wave packets seem to be associated with higher tidal harmonics. Although satellite observations during the same period suggest the presence of a well-organized rank-ordered ISW packet north of the Lombok Strait, the high-frequency wave packets we observed are not rank-ordered. We attribute this effect to the possible interaction of the high-frequency waves with the

sloping topography. Another striking feature is the disappearance of ISW within the fourth observed internal tidal trough while the barotropic forcing is increasing. We have no clear explanation for this observation yet, it is possible that the strong mixing generated at the sill alters the stratification structure and the generation of ISW. It is also possible that stronger nonlinearities, dissipation, 3D effects, and interactions with the Lombok slope disrupt the wave packet structure.

Two turbulence length scales, the Thorpe and Ellison scales, were used to estimate the turbulent dissipation rate from intermittent CTD measurements and high temporal resolution temperature sensors. The dissipation rate ($\varepsilon_{\text{Th-GM}}$, $\varepsilon_{\text{E-GM}}$) in the Lombok Strait thermocline is high of the order of ~[10^{-6}-10^{-7}] m^2s^{-3}, comparable to that observed in other turbulent hot-spot locations such as the north and south Halmahera Straits and the Ombai Strait (Bouruet-Aubertot et al., 2018). The shear measurements made over a limited layer in the upper thermocline show that frequent supercritical conditions are reached. The shear vertical structure is characterized by a small scale of ~20 m with high-frequency variation associated to the high-frequency waves heaving. We also found a clear phasing between the M_2 internal tidal trough and the elevated dissipation rate estimated using both turbulent scales. We suggest investigating the dependence of dissipation rate on the scaled strain in the future to understand the dynamical processes involved (small scale shear layers, high-frequency waves, etc.). This points out the requirement for a specific parameterization of these high-frequency processes.

Our observation site is interesting to characterize the enhanced dissipation induced when the ISWs interact with the shore. Future observations study should focus on the NPS where the 3D hydrostatic model by Nagai and Hibiya (2015) (**Figure 1**a) shows the highest dissipation. A transect along the center of the Lombok Strait should also provide some insight into the transformation of the internal tides into ISW while avoiding the complex slope/solitary waves interaction process.

Acknowledgment

This observation was funded by the Indonesian Endowment Fund Scholarship Program (LPDP), Indonesian Ministry of Finance; the program of CNRS LEFE INSU "*Ondes solitaires et*

388 *turbulence dans le detroit de Lombok*" as well as the PHC Nusantara Project, a joint program
389 between Campus France and Indonesian Ministry of Research and Technology (KEMENRISTEK);
390 and Research Center for Oceanography-Indonesian Institute of Sciences (RCO-LIPI). We are also
391 grateful to Kang Hendra Munandar and all staff of Marine Bio-industry Research Station RCO-LIPI
392 Lombok for preparing the accommodations during the field research, and Pak Djatmiko Irianto for
393 fully helping the data acquisitions. The publication of this research is supported by the funding
394 scheme under the Deputy of Earth Sciences of the Indonesian Institute of Sciences (LIPI).

Appendix : Thorpe and Ellison scale processing

Thorpe scale analysis

Our first estimate of the dissipation rate is based on the classical Thorpe method, performed by examining the overturns in the density profiles. The Thorpe scale is defined as the RMS value of the displacements that one needs to apply to re-order an unstable density profile in a stable way (Ferron et al., 1998; Kunze et al., 2006; Park et al., 2014; Thorpe, 1977; Yang et al., 2014). Due to a large noise level observed from the unpumped CTD in the salinity profiles, we prefer to use the temperature-based estimates in this study, as in Mater et al. (2015). To this end, we need to assume that the potential temperature is a good proxy for the potential density. Here, it is a reasonable assumption since 1) considering the temperature and salinity range variation observed, the temperature-induced potential density variation is one order of magnitude larger (4 kg m^{-3}) than the salinity induced variation (0.4 kg m^{-3}), 2) the salinity and temperature variation both agree with to a potential density increase with depth down to about 150 m and 3) although the salinity slightly decreases below 150 m depth, its range of variation below this depth is very weak (~0.03 PSU) compared to the temperature variation (~3°C) resulting in a factor of ~30 between the temperature and salinity induced potential density variation. **Figure 5**a shows the temperature-salinity relationship inferred using the spline fit method with the goodness values are indicated. For the temperature, we set the noise level as 10 times the temperature sensor resolution of the SBE 19 *Seacat Profiler*, $\delta_T = 0.0001 \times 10$ °C. Spurious noise-induced inversions were then eliminated using the intermediate profile method, firstly proposed by Ferron et al. (1998) and later modified by Gargett and Garner (2008). A method proposed by Gargett and Garner (2008) is also applied to reject a suspected false overturn, using the overturn ratio, $R_o=\min(L^+/L, L^-/L)$; where L^+ and L^- are respectively the vertical distances occupied by positive and negative Thorpe displacements within an overturn of vertical extent L. A single perfect overturn should contain equal lengths of positive and negative displacements, hence $R_o = 0.5$, and an imperfect overturn would have R_o less than 0.5. Mostly, false overturns are associated with values of $R_o < 0.2$ (Gargett and Garner, 2008). Following

Dillon (1982), Ferron et al. (1998) and Moum (1996), we assume that L_T has a linear relationship with the Ozmidov scale $L_O = 0.8\ L_T$, where $L_O = (\varepsilon N^{-3})^{1/2}$, so that we get finally:

$$\varepsilon_{Th} = 0.64 L_T^{\,2} N^3 \tag{1}$$

where N is the mean buoyancy frequency of the 2.5 m sliding mean in the overturn patch region, defined as

$$N^2 = \frac{g}{\rho_0}\frac{d\rho}{dz} \tag{2}$$

The Thorpe scale method provides dissipation rate estimates when density overturns or turbulent fluctuations overcome the noise level or spurious process contamination (surface waves, mooring line motion). As a result, the statistics of dissipation rate are biased toward high values when no assumption is made for the main portion of the water column where no density overturns or turbulent fluctuations are detected. For this section, we assume a lower bound background dissipation rate from a fine-scale parameterization for internal waves. Briefly, the TKE dissipation rate is estimated as (Purwandana et al., 2020),

$$\varepsilon_{Th\text{-}GM} = \begin{cases} 0.64 L_T^{\,2} N^3, & \text{when there is overturn} \\ \max\left(1\times10^{-10}\,\mathrm{m^2 s^{-3}},\ \varepsilon_0\left(\dfrac{N^2}{N_0^{\,2}}\right)\right), & \text{when no overturn observed} \end{cases} \tag{5}$$

1×10^{-10} is the typical minimum dissipation rate observed by microstructure measurements in a quiet region, the Banda Sea (Alford et al., 1999; Bouruet-Aubertot et al., 2018; Koch-Larrouy et al., 2015); $\varepsilon_0 = 7\times10^{-10}\ \mathrm{m^2 s^{-3}}$ and $N_0 = 3$ cph is the canonical Garret and Munk (hereinafter GM) dissipation rate and buoyancy frequency reference, respectively; $\varepsilon_0(N^2/N_0^2)$ is the GM-background dissipation rate given by the fine-scale parameterization for internal waves (Gregg, 1989) yet assuming that the local shear variance S_{10}^2 is equal to the canonical shear variance S_{GM}^2 due to lack of shear measurements over the whole water column. This improved dissipation rate estimate that

takes into account the background dissipation rate is termed $\varepsilon_{Th\text{-}GM}$, and provides continuous profiles of dissipation rates as opposed to the standard Thorpe method, ε_{Th}.

Ellison scale analysis

The high-resolution temporal resolution of the temperature time series allows us to use an alternative proxy of the dissipation rate that is based on the Ellison scale. It scales the vertical distance traveled by fluctuating density/temperature from its vertical gradient of the mean density/temperature (Moum, 1996). In our case, the Ellison scale is estimated from horizontal profiles of temperature time series hence omitting the influence of vertical oscillation due to internal and surface waves is important to diminish spurious turbulence.

First, as was done for the Thorpe scale, we assume that the potential temperature is a good proxy for the potential density and we define the Ellison scale (L_E) as (Cimatoribus et al., 2014)

$$L_{\mathrm{E}} = \overline{(\theta'^2)}^{1/2} / \left(d\bar{\theta}/_{dz} \right) \tag{3}$$

with θ' is the potential temperature fluctuation around the (time) mean value. Note that the temperature time series is filtered to consider only the fluctuation expected to characterize turbulent events as described in detail as follows.

As in Cimatoribus et al. (2014), we define θ' as the potential temperature turbulent fluctuation around the (time) mean value. In a well-controlled experiment, Cimatoribus et al. (2014) have compared the Thorpe and Ellison scales and demonstrated that they fall within a factor of two. If we want L_{E} to be representative of turbulent overturns length scale, θ' must be representative of turbulent fluctuations, hence we need to define the mean value carefully to avoid internal wave contamination in the temperature fluctuations (Cimatoribus et al., 2014; Itsweire et al., 1986). This was done through a high pass wavelet filtering in Cimatoribus et al. (2014) with a cut-off frequency $f_c \cong 1/600$ Hz, here we chose to simply apply a high pass 8th order Butterworth filter with a much higher cut-off frequency $f_c = 1/60$ Hz. We chose this value to smooth as much as possible

462 temperature fronts associated with the non-linear high-frequency internal waves packet while
463 preserving high-frequency turbulent fluctuations. The large ratio of 10 between the cut-off
464 frequency of Cimatoribus et al. (2014) and our study roughly matches the ratio of the buoyancy
465 frequency N in the two experiments, i.e. $N \cong 1\times10^{-4}$ rad s^{-1} in the low stratified environment of
466 Cimatoribus et al. (2014) and $N \cong 2\times10^{-3}$ rad s^{-1} in our strongly stratified environment. Our cut-off
467 value is also close to the lower bound defining the turbulent inertial-convective sub-range chosen by
468 Zhang and Moum (2010) on an equatorial mooring where the stratification is comparable to the
469 Lombok Strait stratification. Zhang and Moum (2010) outlined the contamination of the
470 temperature fluctuations by strong surface waves pumping of their mooring. They eliminated this
471 contamination using its signature on the cross-correlation between the accelerometers and the
472 temperature signal. During our experiment, the conditions were almost flat, yet a close examination
473 of the temperature signal and spectra revealed the occasional signature of contamination by surface
474 waves in the form of oscillation at a period of ~0.1 Hz and an associated spectral peak. Lacking
475 accelerometers, we derive an empirical criterion to eliminate these portions of the signal. We
476 compute the spectral density $S(f)$ of the de-trended θ over 2000 s windows. The valuable frequency
477 range related to the turbulent fluctuations is set >1/60 Hz and we define the frequency range
478 possibly related to the contamination by the surface wave within a frequency of [1/15 – 1/8] Hz. A
479 reference fitted spectrum $S_R(f)$ is then built by a power-law fitting of the temperature spectrum $S(f)$
480 omitting points in the possibly contaminated range [1/15 – 1/8] Hz. Finally, the ratio $r = \int_{1/12}^{1/6} S(f)df / \int_{1/12}^{1/6} S_R(f)df$ of the variance of the signal in the surface waves frequency band
482 between the fitted and observed spectrum is computed.

483 By visual inspection of the spectra $S(f)$ and corresponding time series, we determined that
484 surface wave contamination was not detectable for $r > 0.6$, with this criteria, 20% of the data were
485 rejected. Figure A1 shows an example of the rejected spectrum and the accepted spectrum.

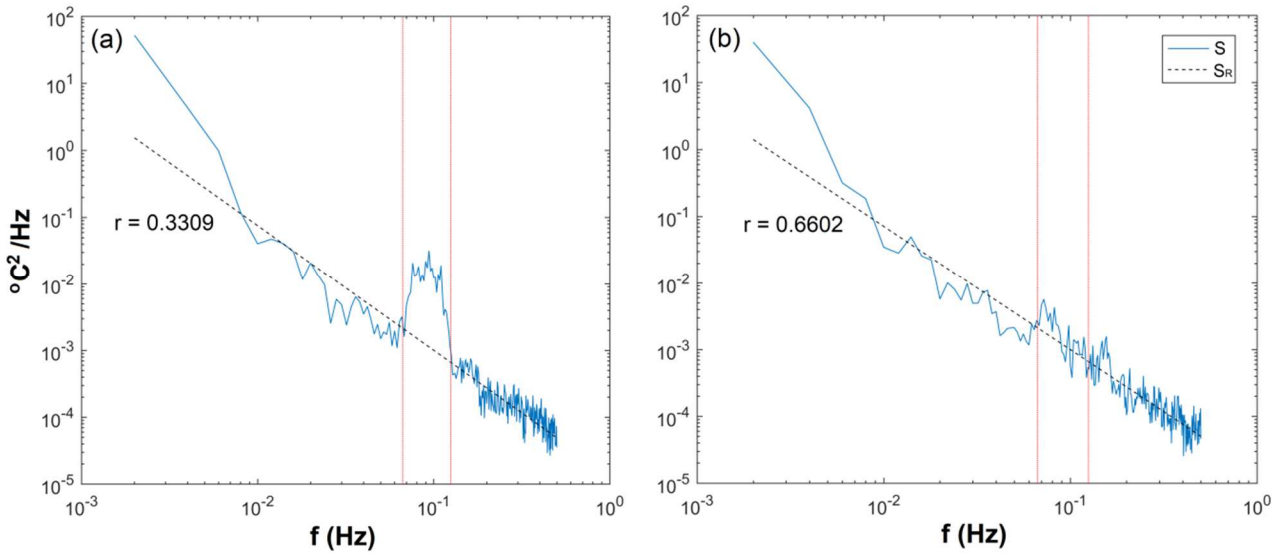

Figure A1 Spectrum of temperature fluctuations showing (a) contaminated by surface waves (r = 0.3309) and (b) uncontaminated by surface waves (r = 0.6602). The black dashed line represents the power-law fit $S_R(f)$ (see text for details). The red dashed lines mark the [1/15, 1/8] Hz which is the frequency band of possible surface waves.

An important source of error is the estimation of $d\overline{\theta}/dz$. Indeed, we estimate the mean temperature gradient from the temperature difference between successive temperature sensors. Since these sensors are separated by a large distance of 40 m on average, this estimate may not represent the local gradient. Following the method of Moum et al. (2011), an estimation of this local gradient can be obtained when surface waves dominate the signal over their frequency band Bw = [1/15, 1/8] Hz. Indeed, in this case, most of the temperature fluctuations generated in the range Bw results from vertical oscillations of the temperature sensors induced by the surface wave pumping of the mooring, as this is the case spectrum shown in **Figure A1**a. The local temperature gradient can then be obtained by filtering the temperature and pressure/depth fluctuations in the range Bw and fitting θ against z to get the local slope $d\overline{\theta}/dz$. This was done for successive sequences of 120 s. An example of such a fit is shown in **Figure A2**.

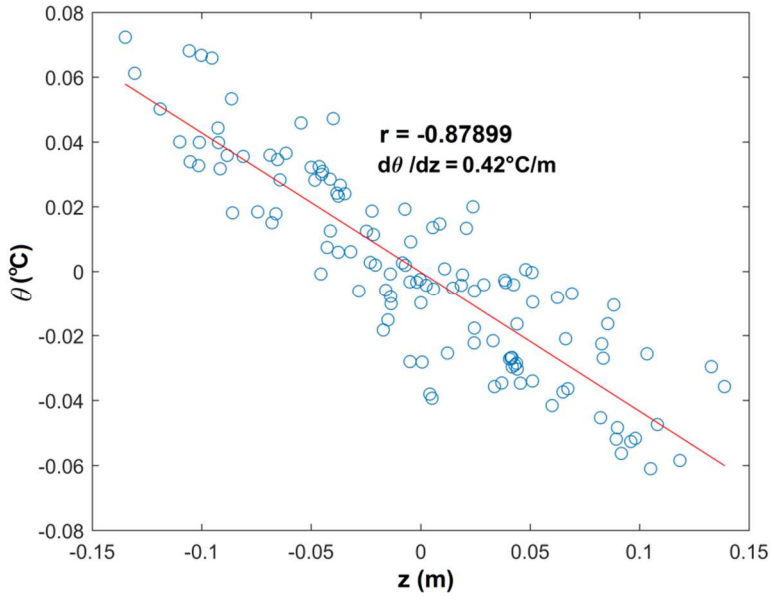

502

503 **Figure A2** Fluctuations of temperature in the band *Bw* = [1/15, 1/8] Hz as a function of the sensor
504 depth for a time sequence where *Bw* is dominated by surface waves.

505 This local estimate $\bar{\theta}_{z,local}$ can only be computed when surface waves dominate the
506 frequency band *Bw*, that is ~20% of the time, but it can be used to estimate the dispersion between
507 the local temperature gradient and the one based on the temperature difference between two sensors
508 $\acute{\theta}_{z,diff}$. The comparison is shown in Figure A3. We can see that although there is an important
509 dispersion yet there is no systematic bias between the two estimates. We find that 90% of $\bar{\theta}_{z,local}$
510 values are within [0.28, 4.6] $\bar{\theta}_{z,diff}$ (marked by white dashed lines in Figure A3a). The dispersion
511 for the $\log_{10}$ of the ratio $x = log_{10}(\bar{\theta}_{z,diff}/\bar{\theta}_{z,local})$ is close to Gaussian with a close to zero mean
512 value of x = -0.017 and a standard deviation σ_x = 0.55 (Figure A3b). In the following, we use this
513 Gaussian fit to compute the confidence interval on $\bar{\theta}_{z,diff}$ and the resulting error on the
514 computation of the Ellison scale and derived dissipation rate. Then, the Ellison scale, L_E is
515 calculated using Eq. (3), and eventually, we determine the turbulent dissipation rate as:

$$\varepsilon_E = {L_E}^2 N^3 \qquad (4)$$

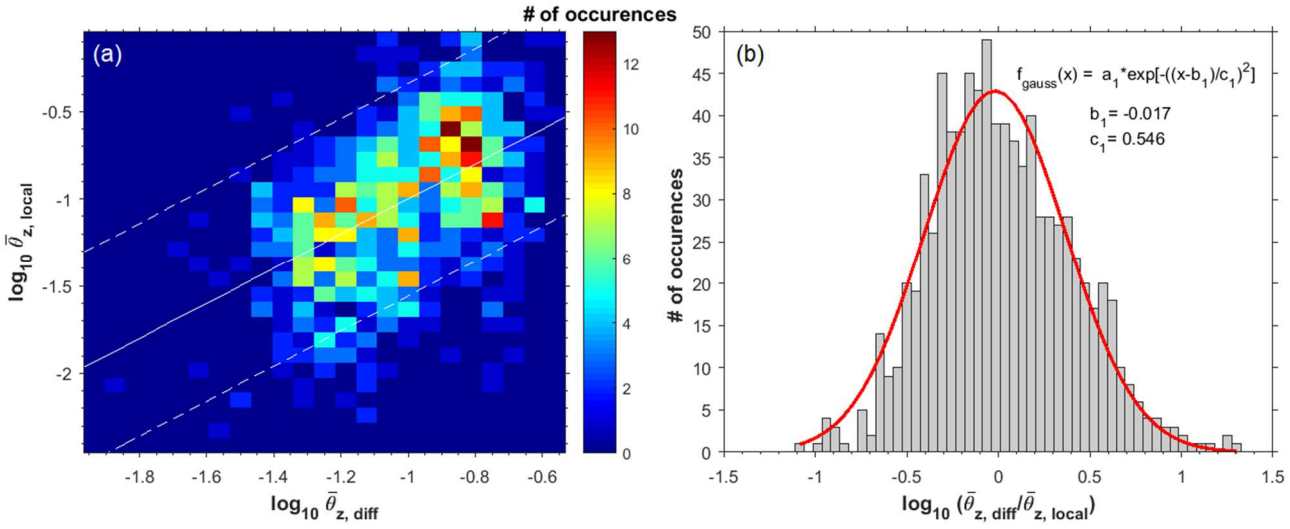

Figure A3 (a) Number of occurrences plot in bins of $\log_{10} \bar{\theta}_{z,diff}$ and $\log_{10} \bar{\theta}_{z,local}$, (b) distribution of $x = log_{10}(\bar{\theta}_{z,diff}/\bar{\theta}_{z,local})$ and its Gaussian fit. The white dashed lines in (a) represent 90% of $\bar{\theta}_{z,local}$ values are within [0.28, 4.6] $\bar{\theta}_{z,diff}$.

References

Aiki, H., Matthews, J.P., Lamb, K.G., 2011. Modeling and energetics of tidally generated wave trains in the Lombok Strait: Impact of the Indonesian Throughflow. J. Geophys. Res. Ocean. 116. doi:10.1029/2010JC006589

Alford, M.H., Gregg, M.C., Ilyas, M., 1999. Diapycnal mixing in the Banda Sea: Results of the first microstructure measurements in the Indonesian throughflow. Geophys. Res. Lett. 26, 2741–2744. doi:10.1029/1999GL002337

Alford, M.H., Peacock, T., MacKinnon, J.A., Nash, J.D., Buijsman, M.C., Centurioni, L.R., Chao, S.-Y., Chang, M.-H., Farmer, D.M., Fringer, O.B., Fu, K.-H., Gallacher, P.C., Graber, H.C., Helfrich, K.R., Jachec, S.M., Jackson, C.R., Klymak, J.M., Ko, D.S., Jan, S., Johnston, T.M.S., Legg, S., Lee, I.-H., Lien, R.-C., Mercier, M.J., Moum, J.N., Musgrave, R., Park, J.-H., Pickering, A.I., Pinkel, R., Rainville, L., Ramp, S.R., Rudnick, D.L., Sarkar, S., Scotti, A., Simmons, H.L., St Laurent, L.C., Venayagamoorthy, S.K., Wang, Y.-H., Wang, J., Yang, Y.J., Paluszkiewicz, T., (David) Tang, T.-Y., 2015. The formation and fate of internal waves in the

South China Sea. Nature 521, 65–69. doi:10.1038/nature14399

Apel, J.R., Holbrook, J.R., Liu, A.K., Tsai, J.J., 1985. The Sulu Sea Internal Soliton Experiment. J. Phys. Oceanogr. doi:10.1175/1520-0485(1985)015<1625:TSSISE>2.0.CO;2

Astawa Karang, I.W.G., Nishio, F., Mitnik, L., Osawa, T., 2012. Spatial-Temporal Distribution and Characteristics of Internal Waves in the Lombok Strait Area Studied by Alos-Palsar Images. Earth Sci. Res. 1, 11–22. doi:10.5539/esr.v1n2p11

Bourgault, D., Morsilli, M., Richards, C., Neumeier, U., Kelley, D.E., 2014. Sediment resuspension and nepheloid layers induced by long internal solitary waves shoaling orthogonally on uniform slopes. Cont. Shelf Res. 72, 21–33. doi:10.1016/j.csr.2013.10.019

Bouruet-Aubertot, P., Cuypers, Y., Ferron, B., Dausse, D., Ménage, O., Atmadipoera, A., Jaya, I., Olivier, M., Atmadipoera, A., Jaya, I., 2018. Contrasted turbulence intensities in the Indonesian Throughflow: a challenge for parameterizing energy dissipation rate. Ocean Dyn. 68, 1–75. doi:10.1007/s10236-018-1159-3

Brandt, P., Romeiser, R., Rubino, A., 1999. On the determination of characteristics of the interior ocean dynamics from radar signatures of internal solitary waves. J. Geophys. Res. Ocean. 104, 30039–30045. doi:10.1029/1999JC900092

Cimatoribus, A.A., Van Haren, H., Gostiaux, L., 2014. Comparison of Ellison and Thorpe scales from Eulerian ocean temperature observations. J. Geophys. Res. Ocean. 119, 7047–7065. doi:10.1002/2014JC010132

Dillon, T.M., 1982. Vertical overturns: A comparison of Thorpe and Ozmidov length scales. J. Geophys. Res. 87, 9601. doi:10.1029/JC087iC12p09601

Egbert, G.D., Erofeeva, S.Y., 2002. Efficient Inverse Modeling of Barotropic Ocean Tides. J. Atmos. Ocean. Technol. 19, 183–204. doi:10.1175/1520-0426(2002)019<0183:EIMOBO>2.0.CO;2

558 Ferron, B., Mercier, H., Speer, K., Gargett, A., Polzin, K., 1998. Mixing in the Romanche Fracture
559 Zone. J. Phys. Oceanogr. 28, 1929–1945. doi:10.1175/1520-
560 0485(1998)028<1929:MITRFZ>2.0.CO;2

561 Ffield, A., Gordon, A.L., 1996. Tidal mixing signatures in the Indonesian seas. J. Phys. Oceanogr.
562 doi:10.1175/1520-0485(1996)026<1924:TMSITI>2.0.CO;2

563 Ffield, A., Robertson, R., 2008. Temperature finestructure in the Indonesian seas. J. Geophys. Res.
564 Ocean. 113, 1–19. doi:10.1029/2006JC003864

565 Gargett, A., Garner, T., 2008. Determining Thorpe scales from ship-lowered CTD density profiles.
566 J. Atmos. Ocean. Technol. 25, 1657–1670. doi:10.1175/2008JTECHO541.1

567 Gerkema, T., Zimmerman, J.T.F., 1995. Generation of Nonlinear Internal Tides and Solitary Waves.
568 J. Phys. Oceanogr. 25, 1081–1094. doi:10.1175/1520-
569 0485(1995)025<1081:GONITA>2.0.CO;2

570 Gordon, A.L., 2005. Oceanography of the Indonesian Seas and their throughflow. Oceanography
571 18, 14–27. doi:10.5670/oceanog.2005.18

572 Gordon, A.L., Fine, R.A., 1996. Pathways of water between the Pacific and Indian oceans in the
573 Indonesian seas. Nature 379, 146–149. doi:10.1038/379146a0

574 Gregg, M.C., 1989. Scaling turbulent dissipation in the thermocline. J. Geophys. Res. Ocean. 94,
575 9686–9698. doi:10.1029/JC094iC07p09686

576 Hatayama, T., 2004. Transformation of the Indonesian throughflow water by vertical mixing and its
577 relation to tidally generated internal waves. J. Oceanogr. 60, 569–585.
578 doi:10.1023/B:JOCE.0000038350.32155.cb

579 Hautala, S.L., Reid, J.L., Bray, N., 1996. The distribution and mixing of Pacific water masses in the
580 Indonesian Seas. J. Geophys. Res. 101, 12,375-12,389. doi:10.1029/96JC00037

581 Hautala, S.L., Sprintall, J., Potemra, J.T., Chong, J.C., Pandoe, W., Bray, N., Ilahude, a. G., 2001.

582 Velocity structure and transport of the Indonesian Throughflow in the major straits restricting
583 flow into the Indian Ocean. J. Geophys. Res. 106, 19527. doi:10.1029/2000JC000577

584 Holloway, P., Pelinovsky, E., Talipova, T., 2002. Internal Tide Transformation and Oceanic Internal
585 Solitary Waves BT - Environmental Stratified Flows, in: Grimshaw, R. (Ed.), . Springer US,
586 Boston, MA, pp. 29–60. doi:10.1007/0-306-48024-7_2

587 Itsweire, E.C., Helland, K.N., Van Atta, C.W., 1986. The evolution of grid-generated turbulence in a
588 stably stratified fluid. J. Fluid Mech. 162, 299–338. doi:10.1017/S0022112086002069

589 Jackson, C., 2007. Internal wave detection using the Moderate Resolution Imaging
590 Spectroradiometer (MODIS). J. Geophys. Res. 112, C11012. doi:10.1029/2007JC004220

591 Klymak, J.M., Pinkel, R., Rainville, L., 2008. Direct Breaking of the Internal Tide near Topography:
592 Kaena Ridge, Hawaii. J. Phys. Oceanogr. 38, 380–399. doi:10.1175/2007JPO3728.1

593 Koch-Larrouy, A., Atmadipoera, A., van Beek, P., Madec, G., Aucan, J., Lyard, F., Grelet, J.,
594 Souhaut, M., 2015. Estimates of tidal mixing in the Indonesian archipelago from
595 multidisciplinary INDOMIX in-situ data. Deep. Res. Part I Oceanogr. Res. Pap. 106, 136–153.
596 doi:10.1016/j.dsr.2015.09.007

597 Koch-Larrouy, A., Lengaigne, M., Terray, P., Madec, G., Masson, S., 2010. Tidal mixing in the
598 Indonesian seas and its effect on the tropical climate system. Clim. Dyn. 34, 891–904.
599 doi:10.1007/s00382-009-0642-4

600 Koch-Larrouy, A., Madec, G., Bouruet-Aubertot, P., Gerkema, T., Bessières, L., Molcard, R., 2007.
601 On the transformation of Pacific Water into Indonesian Throughflow Water by internal tidal
602 mixing. Geophys. Res. Lett. 34. doi:10.1029/2006GL028405

603 Kunze, E., Firing, E., Hummon, J.M., Chereskin, T.K., Thurnherr, A.M., 2006. Global Abyssal
604 Mixing Inferred from Lowered ADCP Shear and CTD Strain Profiles. J. Phys. Oceanogr. 36,
605 1553–1576. doi:10.1175/JPO2926.1

606 Lee, T., Fukumori, I., Menemenlis, D., Xing, Z.F., Fu, L.-L., 2002. Effects of the Indonesian
607 Throughflow on the Pacific and Indian oceans. J. Phys. Oceanogr. 32, 1404–1429.
608 doi:10.1175/1520-0485(2002)032<1404:Eotito>2.0.Co;2

609 Mater, B.D., Venayagamoorthy, S.K., St. Laurent, L., Moum, J.N., 2015. Biases in Thorpe-Scale
610 Estimates of Turbulence Dissipation. Part I: Assessments from Large-Scale Overturns in
611 Oceanographic Data. J. Phys. Oceanogr. 45, 2497–2521. doi:10.1175/JPO-D-14-0128.1

612 Matthews, J.P., Aiki, H., Masuda, S., Awaji, T., Ishikawa, Y., 2011. Monsoon regulation of Lombok
613 Strait internal waves. J. Geophys. Res. Ocean. 116, 1–14. doi:10.1029/2010JC006403

614 Maxworthy, T., 1979. A note on the internal solitary waves produced by tidal flow over a three-
615 dimensional ridge. J. Geophys. Res. 84. doi:10.1029/JC084iC01p00338

616 Moum, J.N., 1996. Energy-containing scales of turbulence in the ocean thermocline. J. Geophys.
617 Res. Ocean. 101, 14095–14109. doi:10.1029/96JC00507

618 Moum, J.N., Nash, J.D., Smyth, W.D., 2011. Narrowband oscillations in the upper equatorial
619 Ocean. Part I: Interpretation as shear instabilities. J. Phys. Oceanogr. 41, 397–411.
620 doi:10.1175/2010JPO4450.1

621 Murray, S.P., Arief, D., 1988. Throughflow into the Indian Ocean through the Lombok Strait,
622 January 1985–January 1986. Nature 333, 444–447. doi:10.1038/333444a0

623 Nagai, T., Hibiya, T., 2015. Internal tides and associated vertical mixing in the Indonesian
624 Archipelago. J. Geophys. Res. C Ocean. 3373–3390. doi:10.1002/2014JC010592

625 Nagai, T., Hibiya, T., Bouruet-Aubertot, P., 2017. Nonhydrostatic Simulations of Tide-Induced
626 Mixing in the Halmahera Sea: A Possible Role in the Transformation of the Indonesian
627 Throughflow Waters. J. Geophys. Res. Ocean. 122, 8933–8943. doi:10.1002/2017JC013381

628 Nugroho, D., Koch-larrouy, A., Gaspar, P., Lyard, F., Re, G., Tranchant, B., 2018. Modelling
629 explicit tides in the Indonesian seas : An important process for surface sea water properties.

630 Mar. Pollut. Bull. doi:10.1016/j.marpolbul.2017.06.033

631 Park, Y.H., Lee, J.H., Durand, I., Hong, C.S., 2014. Validation of Thorpe-scale-derived vertical
632 diffusivities against microstructure measurements in the Kerguelen region. Biogeosciences 11,
633 6927–6937. doi:10.5194/bg-11-6927-2014

634 Polzin, K.L., Naveira Garabato, A.C., Huussen, T.N., Sloyan, B.M., Waterman, S., 2014. Finescale
635 parameterizations of turbulent dissipation. J. Geophys. Res. Ocean. 119, 1383–1419.
636 doi:10.1002/2013JC008979

637 Potemra, J.T., Hautala, S., Sprintall, J., Pandoe, W., 2002. Interaction between the Indonesian Seas
638 and the Indian Ocean in Observations and Numerical Models *. J. Phys. Oceanogr. 32, 1838–
639 1854. doi:10.1175/1520-0485(2002)032<1838:IBTISA>2.0.CO;2

640 Purwandana, A., Cuypers, Y., Bouruet-Aubertot, P., Nagai, T., Hibiya, T., Atmadipoera, A.S.A.S.,
641 2020. Spatial structure of turbulent mixing inferred from historical CTD datasets in the
642 Indonesian seas. Prog. Oceanogr. 184, 102312. doi:10.1016/j.pocean.2020.102312

643 Ray, R.D., Susanto, R.D., 2016. Tidal mixing signatures in the Indonesian seas from high-resolution
644 sea surface temperature data. Geophys. Res. Lett. 43, 8115–8123. doi:10.1002/2016GL069485

645 Robertson, R., Ffield, A., 2005. M2 Baroclinic Tides in the Indonesian Seas. Oceanography 18, 62–
646 73. doi:10.5670/oceanog.2005.06

647 Schiller, A., 2004. Effects of explicit tidal forcing in an OGCM on the water-mass structure and
648 circulation in the Indonesian throughflow region. Ocean Model. 6, 31–49. doi:10.1016/S1463-
649 5003(02)00057-4

650 Scotti, A., Beardsley, R.C., Butman, B., 2007. Generation and propagation of nonlinear internal
651 waves in Massachusetts Bay 112, 1–19. doi:10.1029/2007JC004313

652 Sprintall, J., Chong, J., Syamsudin, F., Morawitz, W., Hautala, S., Bray, N., Wijffels, S., 1999.
653 Dynamics of the South Java Current in the Indo-Australian Basin. Geophys. Res. Lett. 26,

654 2493–2496. doi:10.1029/1999GL002320

655 Sprintall, J., Potemra, J.T., Hautala, S.L., Bray, N.A., Pandoe, W.W., 2003. Temperature and salinity
656 variability in the exit passages of the Indonesian Throughflow. Deep. Res. Part II Top. Stud.
657 Oceanogr. 50, 2183–2204. doi:10.1016/S0967-0645(03)00052-3

658 Susanto, R.D., Gordon, L., Zheng, Q., 2001. Upwelling along the coasts of Java and Sumatra and its
659 relation to ENSO. Geophys. Res. Lett. 28, 1599–1602. doi:10.1029/2000GL011844

660 Susanto, R.D., Mitnik, L., Zheng, Q., 2005. Ocean Internal Waves Observed in the Lombok Strait.
661 Oceanography 18, 80–87. doi:10.5670/oceanog.2005.08

662 Thorpe, S.A., 1977. Turbulence and Mixing in a Scottish Loch. Philos. Trans. R. Soc. A Math. Phys.
663 Eng. Sci. 286, 125–181. doi:10.1098/rsta.1977.0112

664 Vlasenko, V., Sanchez Garrido, J.C., Stashchuk, N., Garcia Lafuente, J., Losada, M., 2009. Three-
665 Dimensional Evolution of Large-Amplitude Internal Waves in the Strait of Gibraltar. J. Phys.
666 Oceanogr. 39, 2230–2246. doi:10.1175/2009jpo4007.1

667 Wijffels, S., Sprintall, J., Fieux, M., Bray, N., 2002. The JADE and WOCE I10 / IR6 Throughflow
668 sections in the southeast Indian Ocean. Part 1: water mass distribution and variability. Deep
669 Sea Res. Part II Top. Stud. Oceanogr. 49, 1341–1362. doi:10.1016/S0967-0645(01)00155-2

670 Wyrtki, K., 1961. Physical oceanography of the Southeast Asian waters., Scientific Results of
671 Marine Investigations of the South China Sea and the Gulf of Thailand.
672 doi:10.1017/S0025315400054370

673 Xie, X.H., Cuypers, Y., Bouruet-Aubertot, P., Ferron, B., Pichon, A., Lourenço, A., Cortes, N.,
674 2013. Large-amplitude internal tides, solitary waves, and turbulence in the central Bay of
675 Biscay. Geophys. Res. Lett. 40, 2748–2754. doi:10.1002/grl.50533

676 Yang, Q., Zhao, W., Li, M., Tian, J., 2014. Spatial Structure of Turbulent Mixing in the
677 Northwestern Pacific Ocean. J. Phys. Oceanogr. 44, 2235–2247. doi:10.1175/JPO-D-13-0148.1

678 Zhang, Y., Moum, J.N., 2010. Inertial-Convective subrange estimates of thermal variance
679 dissipation rate from moored temperature measurements. J. Atmos. Ocean. Technol. 27, 1950–
680 1959. doi:10.1175/2010JTECHO746.1